Design, Construction and Testing of a Six-Component Force Balance for the LNEC Wind Tunnel

Francisco Rei Barata Monteiro Vaz
franciscobvaz@tecnico.ulisboa.pt

Instituto Superior Técnico, Universidade de Lisboa, Portugal

December 2025

Abstract

Experimental testing remains a key element in aerodynamic research, with wind tunnels playing a crucial role. The Laboratório Nacional de Engenharia Civil (LNEC) operates several wind tunnels which currently lack dedicated instrumentation for aerodynamic load measurements, limiting their experimental scope. The present work focuses on the development of a six-component aerodynamic force balance to enhance LNEC's experimental capabilities. The force balance was dimensioned according to LNEC's requirements, considering the specifications of its wind tunnels and typical test configurations. The conceptual design was supported by the Analytic Hierarchy Process, enabling a systematic selection of the optimal configuration based on predefined mechanical and practical criteria. The design adopted a Stewart platform configuration, where six sensing bars measure aerodynamic loads through their axial forces. A singularity analysis ensured accurate resolution of all load components, and both analytical and FEM analyses were used to validate the structural design and sizing. Force measurements were implemented using beam-type load cells connected to a National Instruments™ data acquisition system. A dedicated LabVIEW™ interface was developed for real-time visualization and recording. Calibration was carried out in two stages: individual load cell characterization and full-system calibration using the Weighted Least Squares Method with a second-order polynomial model. Four models were tested to ensure the accuracy and reliability of the force balance, while allowing to detect several limitations. The final balance demonstrated an accurate and repeatable six-component load measurement, modernizing LNEC's wind tunnel facilities and supporting future aerodynamic research.

Keywords: Six-component aerodynamic force balance, Experimental aerodynamics, Wind tunnel testing, Mechanical design, Load cell instrumentation, Metrological Calibration

1. Introduction

Wind tunnels are among the most important facilities for experimental aerodynamic testing, allowing controlled and repeatable study of scale models. Despite the growing use of computational fluid dynamics, wind tunnel testing remains essential for validating aerodynamic performance and detecting complex flow phenomena that simulations may overlook. To obtain meaningful data, it is crucial for wind tunnels to be equipped with accurate instrumentation.

At the Laboratório Nacional de Engenharia Civil (LNEC), wind tunnels are used for multiple purposes within civil engineering, namely testing the aerodynamic stability of bridges, analysing the behaviour of building structures and façade elements, study the conditions of comfort and pedestrian safety in open spaces, evaluating the vibrations induced on tower and chimney structures, as well as applications in aeronautical or automotive engineering. However, the existing infrastructure lacks an adequate aerodynamic force balance to measure aerodynamic forces and moments, limiting its ability to conduct complete aerodynamic studies. Commercial multi-component balances are often expensive or unsuited with specific requirements, motivating the development of a custom, adaptable, and cost-effective instrument.

The main objective of this work is to design, build, calibrate and test a six-component aerodynamic force balance capable of measuring the three force components and the three moment components. The instrument is intended to be easily adaptable to different models and testing configurations, expanding the experimental capabilities of LNEC's facilities.

2. Background

2.1. Experimental Aerodynamics

Aerodynamics has been developed and studied using three overlapping domains: theoretical, experimental and computational. Despite major advances in computational methods, wind tunnel testing continues to play a crucial role in validating numerical models and studying flow phenomena that cannot be fully captured through simulation.

The purpose of wind tunnels is to provide controlled environments where airflows can be reproduced in a steady and repeatable manner. Depending on their configuration, they can be classified as open or closed circuit tunnels. Open circuit tunnels are simpler and less expensive, suitable for visualizations and low-speed testing, while closed circuit tunnels, such as the aeronautical wind tunnel at LNEC, shown in Figure 1, provide greater flow quality and energy efficiency. Test sections can also be open or closed, and their geometry influences both the aerodynamic accuracy and accessibility for model instrumentation [1].

Figure 1: Aeronautical wind tunnel at LNEC.

2.2. Force Balances

Force balance is the term given to an instrument designed to measure forces and moments.

Depending on the configuration, force balances can be separated into two broad categories: internal and external. While internal force balances are placed inside the test model, requiring a custom design for each model, external force balances are connected to the model using a support structure, increasing the adaptability of the design [1].

Within the various types of external force balances, the platform balances represent one of the most common types. Particularly, the Stewart platform based designs, which adapt the Stewart platform parallel manipulator into a load measurement device, are highly regarded for their versatility and capacity to measure all six force and moment components, making them ideal for modern experimental applications. The generic design of a Stewart platform is constituted by two separate platforms connected by 6 bars, using spherical joints. Among several configurations, Stewart platform tend to be of one of three types: type 3-3, type 3-6 and type 6-6, as shown in Figure 2. The latter is the most generic, since it describes any platform with six vertices in each of the platforms [2].

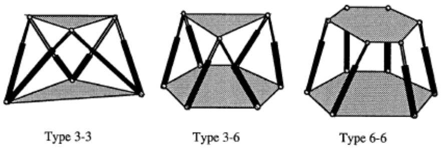

Figure 2: Different types of Stewart platforms.

The difference between the manipulator and the force balance can be found in the bars, where the former employs linear actuators and the latter uses load sensors fitted to each of the bars. As the bars are linearly independent, the resulting mechanism can accurately measure the six components of any applied load.

3. Requirements

To ensure that the force balance met the LNEC's needs, a set requirements was defined, taking into account various constraints and the expected testing scenarios.

3.1. Concept Selection

An Analytic Hierarchy Process (AHP) was used to select the optimal force balance concept. AHP is a multi-criteria decision analysis technique that enables systematic evaluation of different design alternatives by comparing them pairwise against weighted criteria, using both quantitative and qualitative measurements, ensuring a transparent selection process [3].

Six external force balance candidate designs were evaluated: platform, rotating platform, pyramidal, pyramidal platform and two inovative solutions. Twelve criteria covering both construction (criteria) and operational (criteria) aspects were chosen to evaluate the design, requiring a pairwise comparison of the criteria to define the respective weights. The final evaluation score revealed the platform force balance to be the most adequate option.

As such, the Stewart platform configuration was chosen, enabling six-degree-of-freedom load measurement with high precision. Among the various types, a 6-6 platform was selected to solve construction and joint challenges associated with simpler triangular configurations. Its geometry is fully defined by the side lengths of the top and bottom platforms, two coefficients controlling vertex placement, and the platform height, a, b, α, β, h, respectively, as presented in Figure 3.

3.2. Reference Frame

A standardized reference frame was defined according to international standards (ISO 1151/2), with the origin at the balance's attachment point, with an upward pointing z-axis and the x-axis aligned and pointing into the incoming flow, as shown in Figure 3. Wind tunnel specifications were also incorporated into the requirements, considering

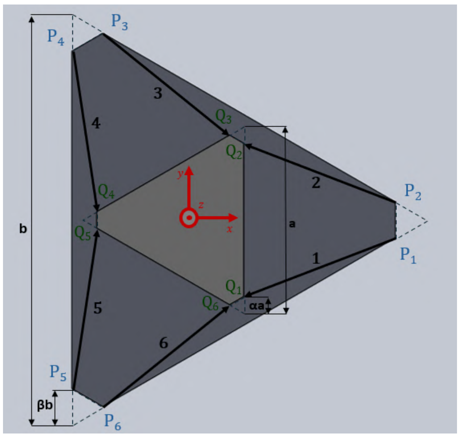

Figure 3: Force balance geometric dimensions and reference frame.

the Aeronautical Wind Tunnel (AWT) [4] and the Boundary Layer Wind Tunnel (BLWT) of LNEC. The informations regarding specific test section dimensions and airspeed limitations were critical to determine the aerodynamic loads on test models used to determine the expected testing scenarios.

3.3. Testing Scenarios

Five representative testing scenarios were analysed: a rectangular flat plate, a half wing model, a Formula Student car model, a suspension bridge section model, and a communications antenna. Aerodynamic coefficients and scaling laws were used to estimate the limiting forces and moments for each case. The results established maximum load requirements as presented in Table 1.

Table 1: Load cases for each testing scenario and corresponding load limits.

Load case	F_x [N]	F_y [N]	F_z [N]	M_x [N·m]	M_y [N·m]	M_z [N·m]
Flat Plate (AWT)	-493	0	0	0	-97	0
Flat Plate (BLWT)	-457	0	0	0	-192	0
Half Wing	-14	333	0	-133	-6	4
FS Car	-177	20	-550	-1	-15	-13
516 Arouca Bridge	-80	0	-8	0	1	0
Antenna	-0.20	0	0	0	-0.04	0
Limit Loads	-493	333	-550	-133	-192	-13

3.4. Displacement Limits and Safety Factors

As displacements in the model significantly affect the applied aerodynamic loads, a limit of 2° was set for angular displacements and 10 mm for linear displacements.

Mechanical safety factors were defined using Pugsley's method [5], resulting in a general factor of 1.45, which was applied to the loads for the FEM simulations. Additional safety considerations were applied to the sensing bars to prevent yield and buckling, limiting maximum axial force (500 N) to 60% of the yield force and 70% of the critical buckling force. These requirements collectively ensure the force balance is both mechanically robust and capable of holding the test models at the set desired attitude across all operational scenarios.

4. Instrumentation

The instrumentation is responsible for measuring the axial forces acting on each sensing bar, acquiring, processing and allowing data visualisation during wind tunnel experiments.

Among several load sensor options, beam loads cells were selected for their affordability, adaptability, and broad capacity range, while maintaining compatibility with other load cell alternatives. The selection of the load capacity of the load cells, which directly influence the measurement range, derived from an analytical model, where each testing scenario was introduced considering a minimum and maximum speed. To ensure both high accuracy at low loads and protection under high loads proved to be a challenge using a single load cell, forcing two measurement ranges to be adopted using 5 kg and 50 kg beam load cells (HX711), shown in Figure 4. This configuration provides full spectrum coverage with no effective discontinuity between the two ranges. For the moment, only the 5 kg were acquired and tested.

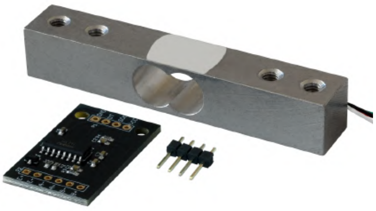

Figure 4: *HX711-05* Load Cell by Simac Electronics GmbH.

Data acquisition was implemented using National Instruments™ *NI-9237* modules installed in a *cDAQ-9178* chassis, capable of processing full Wheatstone bridges with high precision and signal conditioning to amplify the signal and filter any noise present in the signal. The wiring design emphasized modularity and electromagnetic interference prevention, employing DB15 connectors and shielded cables to enable quick sensor replacement and reliable signal transmission.

A dedicated LabVIEW™UI was developed to manage acquisition parameters, display real-time readings, and register data for later post-processing. This integrated system provides accurate, flexible, and user-friendly instrumentation for the aerodynamic force balance, ensuring reliable performance for any user. Additional calibration interfaces were implemented to facilitate systematic load cell and balance calibration.

5. Mechanical Design

The project built upon a pre-existing prototype developed at LNEC, originally based on another force balance design [6]. The goal was to reuse the existing components, namely the two platforms, while redesigning the sensing bars and attachment mechanism to meet the requirements.

5.1. Analytical Model and Singularity Analysis

An analytical model was first established to describe the relationship between the applied aerodynamic loads and the corresponding axial forces in each of the six sensing bars. This model is defined by the main geometric parameters (a, b, α, β, h) which control the spatial configuration of the Stewart platform. Through the coordinates of points P and Q, the pickup points of the bottom and top platforms respectively, the equation of the unit vectors from each of the bars $\vec{V_i}$ are given by

$$\begin{aligned}
\vec{V_1} &= \frac{1}{l}\left(\frac{a - b(2-3\beta)}{2\sqrt{3}}, \frac{a(2\alpha-1)+\beta b}{2}, h\right)\\
\vec{V_2} &= \frac{1}{l}\left(\frac{a - b(2-3\beta)}{2\sqrt{3}}, \frac{a(1-2\alpha)-\beta b}{2}, h\right)\\
\vec{V_3} &= \frac{1}{l}\left(\frac{a(1-3\alpha) - b(3\beta-1)}{2\sqrt{3}}, \frac{a(1-\alpha)-b(1-\beta)}{2}, h\right)\\
\vec{V_4} &= \frac{1}{l}\left(\frac{a(3\alpha-2)+b}{2\sqrt{3}}, \frac{\alpha a-b(1-2\beta)}{2}, h\right)\\
\vec{V_5} &= \frac{1}{l}\left(\frac{a(3\alpha-2)+b}{2\sqrt{3}}, \frac{-\alpha a-b(2\beta-1)}{2}, h\right)\\
\vec{V_6} &= \frac{1}{l}\left(\frac{a(1-3\alpha) - b(3\beta-1)}{2\sqrt{3}}, \frac{a(\alpha-1)-b(\beta-1)}{2}, h\right)
\end{aligned} \tag{1}$$

where l represents the distance between the pickup points.

Using the balance of forces and moments around the attachment point, placed at a certain height d_s above the top platform, the equations for all components of a generic load are given as a function of the axial forces in each sensing bar r_i:

$$F_x = -\sum_{i=1}^{6} r_i \cdot V_{i_x} , \tag{2a}$$

$$F_y = -\sum_{i=1}^{6} r_i \cdot V_{i_y} , \tag{2b}$$

$$F_z = -\sum_{i=1}^{6} r_i \cdot V_{i_z} , \tag{2c}$$

$$M_x = \sum_{i=1}^{6} -r_i \cdot V_{i_z} \cdot Q_{i_y} + \sum_{i=1}^{6} -r_i \cdot V_{i_y} \cdot d_s , \tag{2d}$$

$$M_y = \sum_{i=1}^{6} r_i \cdot V_{i_z} \cdot Q_{i_x} + \sum_{i=1}^{6} r_i \cdot V_{i_x} \cdot d_s , \tag{2e}$$

$$M_z = \sum_{i=1}^{6} r_i \cdot V_{i_x} \cdot Q_{i_y} + \sum_{i=1}^{6} -r_i \cdot V_{i_y} \cdot Q_{i_x} . \tag{2f}$$

The design variables had to be carefully chosen to avoid singularities, which are states where the force balance cannot support one or more of the load's components [7]. To assess the quality of the design, a quality index λ was defined as

$$\lambda = \frac{|J|}{|J|_m} \tag{3}$$

where $|J|$ and $|J|_m$ represent the determinant of the Jacobian matrix of a specific design and of the optimal design respectively. A design with a quality index of 1 represents an optimal design, whereas a design with a quality index of 0 is a design with singularities. The Jacobian matrix is defined as

$$J = \begin{bmatrix} \hat{S}_1 & -\hat{S}_2 & \hat{S}_3 & -\hat{S}_4 & \hat{S}_5 & -\hat{S}_6 \end{bmatrix} , \tag{4a}$$

where

$$\begin{aligned}
\hat{S}_i = \big[& x_{Q_i} - x_{P_i},\ y_{Q_i} - y_{P_i},\ z_{Q_i} - z_{P_i},\ \ldots \\
& y_{P_i} z_{Q_i} - y_{Q_i} z_{P_i},\ x_{P_i} z_{Q_i} - x_{Q_i} z_{P_i},\ x_{P_i} y_{Q_i} - x_{Q_i} y_{P_i} \big]^T
\end{aligned} \tag{4b}$$

which represents the Plucker coordinates of the i^{th} bar, with P and Q represent the vertices of the bottom and top platforms, respectively.

Given that the platforms were pre-existing, only the height could be adjusted. By changing h to 205 mm, compared to the original 250 mm, the quality index increased from 0.916 to 0.997, approaching the ideal condition of the Stewart platform.

5.2. Sensing Bars

The sensing bars, which are critical for both load transmission and measurement, were designed to sustain purely axial loads without yielding or buckling. As such, all of the designed parts for the sensing arms were manufactured using stainless steel (AISI 304), minimizing deformation while avoiding corrosion.

The most important component of the sensing bar is the load sensor, which was created using a beam load cell. A custom adaptor was necessary to allow the beam load cell to measure axial loads, as shown in Figure 5. The adaptor is comprised of two parts: the rod end connector and the lever arm, which transfers the axial load to the opposite end of the load cell, inducing bending stresses that the strain gauges can measure.

To guarantee that the sensing bars only support axial loads, rod end bearings were fitted to each end of the bars. Given that compatibility with existing parts was required, the selection was limited to bearings with holes of 5 mm in diameter. The chosen rod end bearings were the SAKB 5 F and SALKB 5 F from SKF, whose dynamic load rating of 3.25 kN surpass the maximum axial load of 500 N.

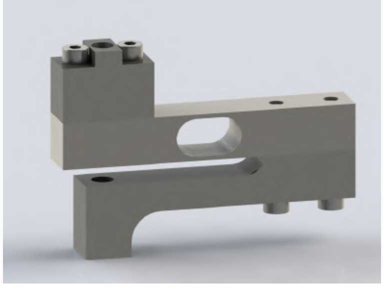

Figure 5: Beam load cell adaptor.

The remaining distance between the pickup points of each platform is bridged with a connecting rod. For the same reasons as the load cell adapter, the chosen material was AISI 304. To ensure compliance with the requirements regarding yield and buckling, the critical diameters required for each of the scenarios to occur with an axial force of 500 N were calculated. For yield the minimum diameter is given by

$$d_{yield} = \sqrt{\frac{4F_{max}}{0.60\pi\sigma_{yield}}}, \quad (5)$$

where F_{max} represents 60% of the maximum force of 500 N [8]. In the case of bucking, a similar process can be followed, calculating the diameter using

$$d_{buckling} = \left(\frac{64F_{max}L^2}{0.70\pi E}\right)^{1/4}, \quad (6)$$

where L represents the distance between the pickup points and E is the Young's modulus of AISI 304 [8]. As the rod's diameter varies between 6 mm and 10 mm, and the achieved values for d_{yield} and $d_{buckling}$ were 2.06 mm and 4.88 mm respectively, the requirements were met.

5.3. Bottom Platform

The bottom platform, already available from the previous prototype, was modified to improve functionality, including the addition of a central hole for the support strut and the application of corrosion protection.

5.4. Top Platform and Support Structure

The top platform, fabricated from a lightweight composite sandwich panel of carbon fibre reinforced polymer and foam core, was retained to combine low mass with high stiffness. However, the entire support structure for the model had to be designed from scratch. All of the bolted connections to the top platform were reinforced with backing plates to prevent the collapse of the foam core.

The flange, which connects the support structure to the top platform, features a three-part aluminium design. It allows the support's position to be adjusted, allowing for changes in the incidence angle of the model as well as its height. A clamping force is provided by one of the three parts, locking the strut into position without damages to the contact surfaces. To ensure a proper contact, a rotating adjustment fit H9d9 was used between the flange's surface and the support's outer wall.

The support structure was designed to provide height, angle of attack, and yaw adjustment capabilities while maintaining minimal deformation under load.

The final force balance design is depicted in Figure 6.

Figure 6: Force balance's final design.

5.5. FEM Analysis

To ensure compliance with the requirements, a FEM analysis was performed on the complete assembly under the defined load cases. The simulations used parabolic tetrahedral elements with a refined curvature-based mesh to refine the mesh in regions of stress concentration, such as the rod end bearings. A mesh convergence study was performed, ensuring a balance between accuracy and computational cost, with a final mesh containing approximately 1.25×10^5 elements. The displacement values at the attachment point for varying element counts, which were used for the study, are shown in Figure 7.

The results confirmed that the design met all displacement and stiffness requirements. The most demanding case corresponded to the flat plate load configuration, whose displacement plot is shown in Figure 8, which produced a maximum linear displacement of 8.12 mm and angular displacement of 1.73°, both within the prescribed limits. These results validated the adequacy of the design and confirmed the overall mechanical robustness of the force balance.

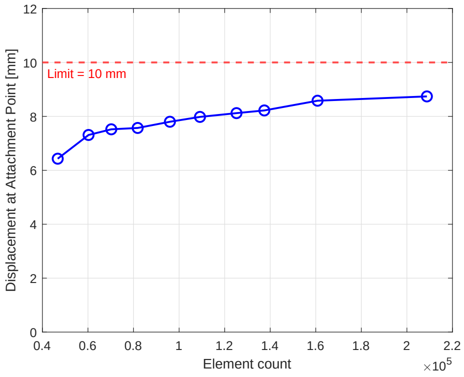

Figure 7: Linear displacements convergence study.

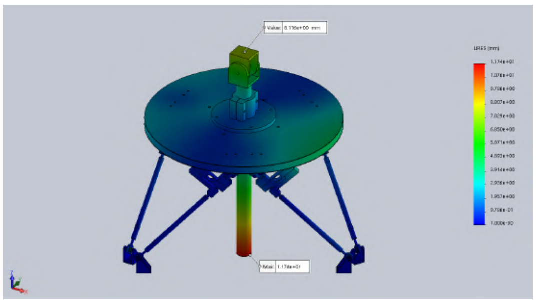

Figure 8: Displacement plot for the plate load case.

6. Calibration

After the assembly of the aerodynamic force balance, a comprehensive calibration procedure was undertaken to establish the relationship between the voltage outputs of the load cells and the aerodynamic loads acting on the balance. The process was divided into two main stages: individual load cell calibration and global force balance calibration.

6.1. Load Cell Calibration

Each load cell was calibrated independently using an dedicated calibration jig, shown in Figure 9, with the goal of obtaining a metrological characterisation for each one. The apparatus consisted of a base plate and a pulley system that allowed the application of both tensile and compressive loads in a controlled and purely axial manner. The calibration procedure involved 21 incremental load steps, from −50 N to +50 N, performed in three complete cycles to assess repeatability and reversibility. The acquired data was used to determine the transfer function between output voltage and axial load through a linear regression, and a full metrological characterisation which followed the recommendations of international standards [9].

Seven main sources of uncertainty were considered: slope, intercept, linearity, reversibility, repeatability, output voltage, and excitation voltage. The condensed uncertainty balance of the load cell with the largest uncertainty is presented in Table 2. The expanded uncertainties (95% confidence) were found to be below 0.4% of full scale for all six load cells, with results proving to be consistent across repetitions. The largest uncertainty contribution originated from the DAQ system's voltage measurement, which was conservatively estimated using datasheet specifications.

Figure 9: Load cell calibration setup.

Table 2: Uncertainty balance for a single load cell.

Sources of uncertainty	DoF	Contribution
Slope	2	0.030 N (9.5%)
Intercept	2	0.017 N (3.0%)
Input Voltage	50	0.056 N (33.2%)
Max Output Voltage	50	0.056 N (33.8%)
Linearity	2	0.042 N (18.6%)
Reversibility	11	0.012 N (1.5%)
Repeatability	23	0.005 N (0.3%)
Standard Load	50	0.001 N (0.0%)
r(m,b)	22	0.002 N (0.0%)
Combined Uncertainty		0.097 N (100.0%)
Effective DoF		37
Expansion Factor		2.03
Expanded Uncertainty (95%)		0.196 N (0.39 %FS)

Despite the simplicity of the beam-type load cells, their performance demonstrated excellent stability and reliability when properly calibrated.

6.2. Force Balance Calibration

The second calibration stage focused on the complete six-component force balance, relating the six bar outputs to the aerodynamic loads applied at the model's attachment point. The process consists in applying N known loads to the force balance creating N calibration points for which a fitting model minimises the errors.

The experimental calibration setup consisted of a dedicated jig designed to allow the application of pure forces, moments as well as combined loads through steel cables, pulleys, and a steel arm connected at the attachment point, as shown in Figure

10.

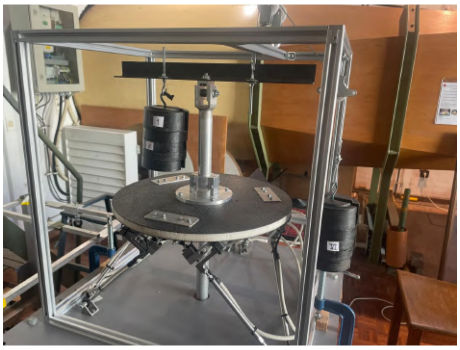

Figure 10: Force balance calibration setup.

A total of 24 load cases containing 178 calibration points in total were used, covering pure forces and moments in all directions, as well as combined loads representative of realistic aerodynamic loading conditions, spanning the entire measurement range of the force balance. Each case was repeated three times to reduce statistical variability, and data acquisition was automated through a custom user interface.

6.2.1. Fitted Model

A second order polynomial model was employed to capture both direct and cross-coupling effects between the sensing bars, improving accuracy over a first order approach. The equation of the fitted model for one of the six load components f_i is given by

$$f_i = \underbrace{\sum_{j=1}^{6} r_j c_{i,j} + \sum_{j=1}^{6}\sum_{k=j}^{6} r_j r_k d_{i,j,k}}_{2^{nd} Order} + \epsilon_i \tag{7}$$

where r represents the axial load on each bars, while c and d represent the calibration coefficients. The loads f_i, where i ranges from 1 to 6, represent $F_x, F_y, F_z, M_x, M_y, M_z$, respectively [10]. This model can be simplified with a single matrix of coefficients $c_{i,j}$, denoted as the calibration matrix, provided that the outputs are given in a single vector R, containing the direct outputs and the cross multiplied outputs:

$$F = CR + \epsilon\,, \tag{8a}$$

with

$$R = \begin{bmatrix} r_1 & r_2 & \dots & r_6 & r_1^2 & r_1 r_2 & \dots & r_6^2 \end{bmatrix}\,. \tag{8b}$$

6.2.2. Weighted Least Squares Method

The calibration coefficients were obtained using the Least Squares Method (LSM), refined through the Weighted Least Squares Method to include the variability and uncertainty of each test. The LSM presents criteria that defines a fitting which minimizes the sum of the squared errors. As such, the estimator of the coefficients matrix can be given by

$$C = (R^T R)^{-1} R^T F\,. \tag{9}$$

The introduction a weighting matrix which places weights on each of the six load components, allows the the fitting model to account for known calibration errors. This diagonal matrix W, of size $N \times N$ can be introduced into the estimator, giving

$$C = (R^T W R)^{-1} R^T W F\,, \tag{10a}$$

with

$$W = V_W + D V_R D^T\,. \tag{10b}$$

The weighting matrix incorporates two main contributions: one associated with the accuracy of the applied loads (V_W), and another related to the uncertainty of the sensing bars ($D V_R D^T$) [10]. The former intends to account for uncertainties in the calibration jig and the weights by introducing the standard deviations of the measured loads on the diagonal of the $N \times N$ matrix. The later assesses the uncertainty of the measured values through the repeatability of the calibration points using matrix V_R, a diagonal symmetric matrix of dimension $6N \times 6N$, where the diagonal entries are the variances between the measurements from each bridge, while the covariances the off diagonal entries. This matrix is multiplied by matrix D, a sensitivity matrix comprised of the partial derivatives of the fitted model.

6.2.3. Goodness of Fit

The quality of the calibration was assessed using the χ^2 goodness of fit criterion, calculated through

$$\chi^2 = (F - \hat{F})^T W^{-1} (F - \hat{F})\,, \tag{11}$$

where $\hat{F}$ represents the fitted loads. A good fit is described by a χ^2 close to the number of degrees of freedom, which represent the independent residuals after fitting the model. As such, a reduced version of χ^2 can be achieved, where a tight fit presents values close to one, using

$$\chi^2_\nu = \frac{\chi^2}{\nu}\,, \tag{12a}$$

where

$$\nu = N - N_c\,, \tag{12b}$$

with $N_c = 27$, the number of coefficients for each load in the fitted model.

The results, shown in Table 3, indicate a clear improvement across iterations, particularly when the weighted LSM was applied, with most load components achieving $\frac{\chi^2}{\nu}$ values close to unity.

Table 3: χ_ν^2 values for various iterations of the weighted LSM.

Load	$W = I$	$W = V_W$	$W = V_W + DV_RD^T$
Fx	2.26	1.36	1.29
Fy	3.36	2.38	2.15
Fz	7.72	6.24	5.25
Mx	0.03	0.03	0.03
My	0.02	0.02	0.02
Mz	0.06	0.05	0.05

6.3. Calibration Results

From the calibration process, a final calibration matrix of dimensions 6 × 27 was achieved. The lines of this matrix represent the fitted equation to each of the load components, where each element represents a coefficient of Equation (7).

Additionally the uncertainty of the calibrated model can assessed by propagating the uncertainties from the load measurements in each bar and the uncertainties of the calibrated model itself [11]. Through the measurement of a calibration load case, presented in Table 4, it is clear that the uncertainties, shown in Table 5, increase with load magnitude, as expected, and that decoupling between different load components remains effective.

Table 4: Fitted loads for a calibration load case.

Load	Fx[N]	Fy[N]	Fz[N]	Mx[N·m]	My[N·m]	Mz[N·m]
1	0.00	0.00	0.00	0.00	0.00	0.00
2	-0.86	-0.01	-1.00	0.00	0.16	0.00
3	-11.53	0.09	-11.57	0.01	1.65	-0.07
4	-21.77	0.17	-21.88	0.02	3.13	-0.10
5	-31.56	0.25	-31.82	0.01	4.64	-0.11
6	-41.15	0.19	-51.57	-0.01	7.63	0.03
7	-49.65	-0.01	-70.35	-0.05	10.74	0.32

Table 5: Combined uncertainties for a calibration load case.

Load	u_{F_x} [N]	u_{F_y} [N]	u_{F_z} [N]	u_{M_x} [N·m]	u_{M_y} [N·m]	u_{M_z} [N·m]
1	0.11	0.12	0.16	0.04	0.04	0.02
2	0.11	0.12	0.17	0.04	0.04	0.02
3	0.13	0.11	0.28	0.07	0.07	0.06
4	0.15	0.12	0.47	0.09	0.10	0.08
5	0.17	0.14	0.67	0.12	0.12	0.10
6	0.26	0.25	1.20	0.20	0.22	0.19
7	0.45	0.45	1.78	0.38	0.41	0.37

7. Testing

Four models were tested to comprehensively assess the accuracy, reliability, and operational behaviour of the developed force balance: a rectangular flat plate, a larger rectangular plate, a flat disk, and a replica of a communications antenna. All of the tests were conducted in the AWT, where the force balance will be mainly used.

7.1. Testing Procedure

The rectangular flat plate served as the primary test model due to its well documented aerodynamic behavior in literature. The model shown in Figure 11, of dimensions 100.7 × 150.7 mm, is fixed at the centroid to the attachment point to ensure it only generates drag and no additional load.

Figure 11: Rectangular flat plate mounted in the AWT.

Tests were performed at air speeds ranging from 5 m/s to 30 m/s, in both ascending and descending directions, to assess linearity and reversibility. To reduce the influence of the added drag provided by the support structure, a fairing was added to shield it from the air flow, as shown in Figure 11.

7.2. Results

The measured drag forces exhibited the expected quadratic dependence on airspeed, as shown in Figure 12, confirming the correct functioning of the balance. The coefficient of determination, R^2, is higher than 0.999, proving that 99.9% of the variations in the drag force provided by variations in the air speed.

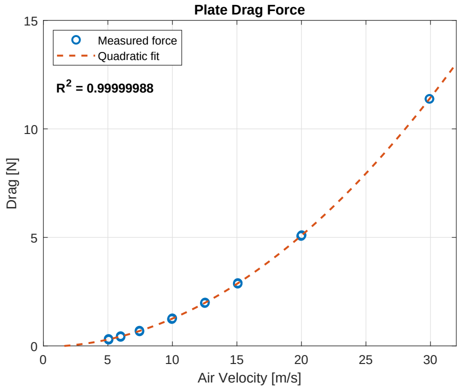

Figure 12: Measured drag force on the flat plate as a function of air speed.

To define the plate's drag coefficient, C_D, the reference area was defined as the frontal area ($S = l \times h$), which in this case has a value of 0.01518 m^2.

When analysed in dimensionless form, the obtained drag coefficients, shown in Figure 13, re-

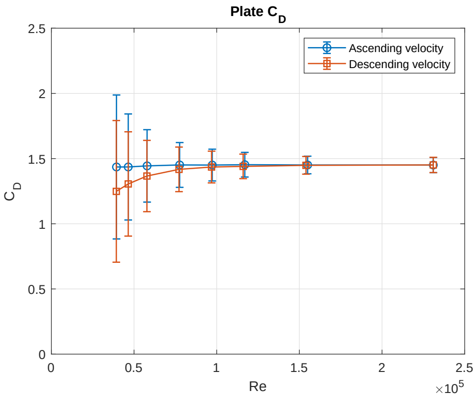

Figure 13: Drag coefficient of the flat plate as a function of *Re*.

mained fairly constant with increasing air speed, as is expected for *Re* of this order os magnitude. However, with decreasing velocities, the coefficient of drag reduces, reaching significant differences at the lowest air speeds, which proved to be a systemic error of the force balance.

Taking the average of the data points acquired with ascending speeds, a value of 1.45 was achieved. Classic references state that, for 3D finite rectangular flat plates, the coefficient tends to fall between 1.1 and 1.3 [12, 13, 14]. The actual value can vary depending on multiple factors, such as aspect ratio, roughness, blockage ratio, among others. However, as the support structure is placed aft of the model, its interference with the airflow can cause a change in the base pressure behind the flat plate, causing an increase in drag, as is demonstrated by several experimental tests [15, 16]. Despite this, the results proved to be consistent, highlighting the accurate and reliable performance of the force balance.

7.3. Operational Considerations

Subsequent tests using the larger plate, disk, and antenna models further highlighted flaws behaviour of the balance and helped to devise strategies to mitigate these.

Tests which produced forces below 0.2 N, exposed the limitations of the system's sensitivity, leading to large uncertainties in the calculated drag coefficients. This emphasised the need for minimum load thresholds during testing.

The systematic and systemic error regarding the measurement discrepancies with decreasing air speeds was also studied conducting multiple consecutive runs using the larger flat plate model, as shown in Figure 14. The results proved that the error was only present on the first run, which could be explained by friction in the rod end bearings. To minimize this affect, it is recommended that, before each test, a short cycle is run to an air speed slightly higher than the maximum intended for the test.

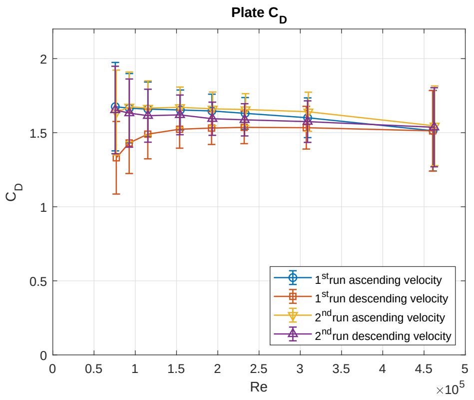

Figure 14: Drag coefficient of the large rectangular plate as a function of *Re*.

Another limitation was the influence of the support structure on the results. The testing of the flat plate models proved that the distance of the plates to the fairing had a significant influence in the drag coefficient, primarily by altering the base pressure distribution behind the plate. By reducing it in half, the drag coefficient of the rectangular flat plate increased by 7%, demonstrating the importance of considering blockage and interference effects when setting up an experimental test.

Dynamic tests conducted with the communications antenna model demonstrated the capability of the balance to capture unsteady aerodynamic phenomena, such as vortex shedding. The results prove that frequencies can be detected in the signal. However, once the model begins to oscillate, the data retrieved does not prove to be reliable to detect shedding frequencies nor validate aerodynamic loads.

8. Conclusions

This work presented the design, development, and calibration of a six-component aerodynamic force balance for LNEC's wind tunnels. The main objective was to create a versatile and accurate measurement system capable of determining all aerodynamic loads while remaining adaptable to different tunnels and testing setups.

The final design, based on the Stewart platform concept, provides structural efficiency and measurement decoupling. Finite element analyses confirmed the balance's stiffness and reliability under the defined operational loads, while efforts were made to minimize component mass and manufacturing cost. Certain reused elements from a previous prototype ensured practical feasibility without compromising performance.

Six commercial beam load cells were integrated as sensing elements, chosen for their precision and flexibility. Their metrological characterisation yielded expanded uncertainties below 0.4% of full scale. A full-system calibration was conducted using a custom jig that applied known loads through weights, cables and pulleys. The calibration employed a second-order polynomial, fitted using the Weighted Least Squares Method, capturing both direct and cross-coupling effects and accounting for sensor uncertainty.

Experimental validation involved four different aerodynamic models tested under various conditions. Results demonstrated consistent and accurate measurements across the full operational range, with deviations mainly attributed to test setup limitations rather than the balance itself.

In conclusion, the developed balance successfully met all design and performance requirements. It provides LNEC with an effective and adaptable tool for precise aerodynamic load measurement, significantly enhancing its experimental and research capabilities.

References

[1] J. B. Barlow, W. H. Rae, and A. Pope. *Low-Speed Wind Tunnel Testing.* John Wiley & Sons, 3rd edition, 1999. ISBN 9780471557746.

[2] B. Dasgupta and T. Mruthyunjaya. The stewart platform manipulator: A review. *Mechanism and Machine Theory*, 35(1):15–40, January 2000. doi:10.1016/S0094-114X(99)00006-3.

[3] O. S. Vaidya and S. Kumar. Analytic hierarchy process: An overview of applications. *European Journal of Operational Research*, 169(1):1–29, February 2006. doi:10.1016/j.ejor.2004.04.028.

[4] A. R. J. Borges. *O túnel aerodinâmico do Laboratório Nacional de Engenharia Civil.*, volume M 319 of *Memórias.* LNEC, 1969.

[5] J. C. Musto. The safety factor: Case studies in engineering judgment. *International Journal of Mechanical Engineering Education*, 38(4):286–296, 2010. doi:10.7227/IJMEE.38.4.2.

[6] M. Ferreira. *Design of a Six-Component External Wind Tunnel Balance.* MSc Thesis in Mechanical Engineering, Instituto Superior Técnico, Lisboa, Portugal, July 2015.

[7] J. Lee. *Investigation of quality indices of in-parallel platform manipulators and development of Web-based analysis tool.* University of Florida, 2000.

[8] R. G. Budynas and J. K. Nisbett. *Shigley's Mechanical Engineering Design.* McGraw-Hill Series in Mechanical Engineering. McGraw-Hill Education, New York, NY, USA, 9th edition, 2011. ISBN 978-0-07-352928-8.

[9] BIPM, IEC, IFCC, ILAC, ISO, IUPAC, IUPAP, and OIML. Evaluation of measurement data — Guide to the expression of uncertainty in measurement. Joint Committee for Guides in Metrology (JCGM), JCGM 100:2008, 2008.

[10] M. Reis, R. Castro, and O. Mello. Calibration uncertainty estimation of a strain-gage external balance. *Measurement*, 46(1):24–33, 2013. doi:10.1016/j.measurement.2012.07.019.

[11] M. L. C. C. Reis, O. A. F. Mello, and S. Uyeno. Calibration uncertainty of an external six-component wind tunnel balance. In *Proceedings of the 33rd AIAA Fluid Dynamics Conference and Exhibit.* American Institute of Aeronautics and Astronautics (AIAA), Orlando, FL, USA, June 2003. doi:10.2514/6.2003-3884.

[12] R. Fail, J. Lawford, and R. Eyre. Low-speed experiments on the wake characteristics of flat plates normal to an air stream. *Aeronautical Research Council Reports & Memoranda*, 3120, 1957.

[13] NASA Glenn Research Center. Shape effects on drag — drag coefficient. Accessed: October 2025.

[14] S. F. Hoerner. *Fluid-Dynamic Drag: Theoretical, Experimental and Statistical Information.* Hoerner Fluid Dynamics, Brick Town, New Jersey, USA, 2nd edition, 1965. ISBN 9991194444. First published 1958 (1st ed.), Library of Congress Catalog Card Number 64-19666.

[15] S. G. Powers, J. K. Huffman, and J. Charles H. Fox. Flight and wind-tunnel measurements showing base drag reduction provided by a trailing disk for high reynolds number turbulent flow for subsonic and transonic mach numbers. NASA Technical Publication (NASA-TP-2638) 2638, National Aeronautics and Space Administration, Scientific and Technical Information Branch, Edwards, California / Hampton, Virginia, USA, November 1986. doi:10.2514/6.2003-3884. Dryden Flight Research Facility, Ames Research Center; Langley Research Center.

[16] B. Hetherington. *Interference of Supports Used for Ground Vehicle Wind Tunnel Testing.* Ph.D. thesis, Durham Thesis, Durham University., (2006).